RESEARCH LETTER

Correspondence to:
M. Müller,
maltem@met.no

Toward an internal gravity wave spectrum in global ocean models

Malte Müller[1,2], Brian K. Arbic[3], James G. Richman[4], Jay F. Shriver[4], Eric L. Kunze[5], Robert B. Scott[6], Alan J. Wallcraft[4], and Luis Zamudio[7]

[1]School of Earth and Ocean Sciences, University of Victoria, Victoria, British Columbia, Canada, [2]Research and Development Department, Norwegian Meteorological Institute, Oslo, Norway, [3]Department of Earth and Environmental Sciences, University of Michigan, Ann Arbor, Michigan, USA, [4]Oceanography Division, Naval Research Laboratory, Stennis Space Center, Hancock County, Mississippi, USA, [5]Northwest Research Associates, Redmond, Washington, USA, [6]Département de Physique, Université de Bretagne Occidentale, Brest, France, [7]Center for Ocean-Atmosphere Prediction Studies, Florida State University, Tallahassee, Florida, USA

Abstract High-resolution global ocean models forced by atmospheric fields and tides are beginning to display realistic internal gravity wave spectra, especially as model resolution increases. This paper examines internal waves in global simulations with 0.08° and 0.04° (~8 and 4 km) horizontal resolutions, respectively. Frequency spectra of internal wave horizontal kinetic energy in the North Pacific lie closer to observations in the 0.04° simulation than in the 0.08° simulation. The horizontal wave number and frequency (K-ω) kinetic energy spectra contain peaks in the semidiurnal tidal band and near-inertial band, along with a broadband frequency continuum aligned along the linear dispersion relations of low-vertical-mode internal waves. Spectral kinetic energy transfers describe the rate at which nonlinear mechanisms remove or supply kinetic energy in specific K-ω ranges. Energy is transferred out of low-mode inertial and semidiurnal internal waves into a broad continuum of higher-frequency and higher-wave number internal waves.

1. Introduction

In this paper, we examine the extent to which high-resolution global ocean models that are simultaneously forced by atmospheric fields and tides [e.g., *Arbic et al.*, 2010, 2012a; *Müller et al.*, 2012] are able to simulate the internal gravity wave spectrum and the extent to which nonlinear internal wave-wave interactions contribute to the simulated spectrum. For about 20 years, basin- and global-scale ocean models have been able to simulate mesoscale eddies with some degree of realism [*McClean et al.*, 1997]. The spectrum of internal gravity waves (hereafter referred to simply as "internal waves") represents a new frontier for global models. Because internal waves redistribute large amounts of energy over long distances, analyses of the global distribution of internal waves and their interactions are relevant to our understanding and simulation of large-scale ocean dynamics [*Munk and Wunsch*, 1998].

Internal wave space-time characteristics in deep water have been represented by a nearly universal spectrum [*Garrett and Munk*, 1975; *Cairns and Williams*, 1976]. The internal wave spectrum covers a range of scales—in time from the buoyancy period (~10 min in the thermocline) to the inertial period (~1 day but depends on latitude), in vertical scale from ~1 m to the ocean depth, and in horizontal scale from ~100 m to greater than 100 km. The internal wave spectrum is fed primarily by near-inertial waves arising from surface wind forcing [e.g., *D'Asaro*, 1984; *Silverthorne and Toole*, 2009; *Simmons and Alford*, 2012] and by internal tides arising from barotropic tidal flow over topography [e.g., *Garrett and Kunze*, 2007]. Nonlinear internal wave-wave interactions have been proposed as the primary mechanism to transfer energy out of the generation frequencies and wave numbers to the broader range of frequencies and wave numbers in the internal wave spectrum [*Müller et al.*, 1986; *Polzin*, 2004]. In an idealized two-dimensional model, with spatial dimensions in the horizontal and vertical that was forced at the near-inertial and semidiurnal frequencies, *Sugiyama et al.* [2009] found that internal wave-wave interactions filled out a frequency wave number spectrum. In the present study, we examine the internal waves and their interactions in realistic three-dimensional global simulations.

A review of nonlinear interactions in the ocean internal wave field by *Müller et al.* [1986] focuses on early theoretical work. The more recent review by *Polzin et al.* [2014] focuses on the development and

application of a practical fine-scale parameterization for turbulent dissipation and mixing based on the energy cascade through the vertical wave number spectrum to small vertical scales. This fine-scale parameterization has found wide use observationally.

Instead of isolating specific triads, as in, for instance, *Sun and Pinkel* [2013] and *MacKinnon et al.* [2013], we will calculate the change in the horizontal kinetic energy spectrum due to nonlinear momentum advection, thus capturing the full range of nonlinear effects at the expense of identifying specific interactions in detail. We will compute horizontal kinetic energy spectra E and nonlinear spectral kinetic energy transfers T in the horizontal wave number-frequency (K-ω) domain based on surface velocities of realistic high-resolution global ocean circulation models forced with atmospheric fields and tides. Note that $K = (k^2 + l^2)^{1/2}$ is the horizontal wave number, with k and l being the zonal and meridional wave numbers, respectively. As discussed further below, our focus on horizontal wave number is due to the availability of surface model fields and the computational difficulty of performing spectral computations with fully three-dimensional high-resolution model output. Our K-ω internal wave spectral transfers are akin to transfers that have long been computed in the horizontal wave number domain for quasi-geostrophic (QG) motions [e.g., *Scott and Wang*, 2005]. *Arbic et al.* [2012b, 2014] extended the spectral analysis of QG kinetic energy transfers to the frequency- and wave number-frequency domains.

In section 2, we introduce the model output and observational data used in this paper. In section 3, the derivation of kinetic energy spectra, E, and spectral energy transfers, T, in (K-ω) space is presented. In section 4, we compare the simulated kinetic energy frequency spectra with spectra from current meter observations. In section 5, we demonstrate that the modeled E and T in (K-ω) space are concentrated along the dispersion relations of low vertical modes. In section 6, we interpret the (K-ω) spectra in terms of triad interactions. A summary is presented in section 7.

2. Model Output and Observational Database

We utilize output in a North Pacific domain spanning 29°N–43°N and 150°W–176°W from two global simulations of the HYbrid Coordinate Ocean Model (HYCOM) [*Chassignet et al.*, 2009]. The model is hydrostatic with 32 layers in the vertical direction. The chosen analysis domain is north of the Hawai'ian Islands in a region of substantial internal tide activity. The nominal horizontal resolutions of the simulations are 0.08° (HYCOM12) and 0.04° (HYCOM25), corresponding to horizontal grid spacing of ~8 and 4 km, respectively. Note that the vertical resolution is the same for both model simulations. The models are forced by astronomical tides and 3-hourly atmospheric fields. As discussed in *Arbic et al.* [2010], the models employ a parameterized topographic internal wave drag and a scalar approximation for the self-attraction and loading term. The spectral calculations in this paper use 6 (3) months of hourly output from HYCOM12 (HYCOM25).

The internal wave spectrum is typically described in terms of frequency and vertical modes [e.g., *Garrett and Munk*, 1975]. However, the volume of three-dimensional output from the HYCOM12 and HYCOM25 simulations is extremely large. Therefore, for computational feasibility, we have chosen to restrict this first analysis of HYCOM internal wave spectra to surface horizontal velocities rather than to three-dimensional velocity fields. The dispersion relations of low vertical modes will be identified in the horizontal wave number-frequency spectra.

The lower-resolution HYCOM12 has been extensively compared to available current meter measurements of the global three-dimensional tidal velocity field [*Timko et al.*, 2013] and to satellite altimetry-constrained estimates of the barotropic and baroclinic components of surface tidal elevations [*Shriver et al.*, 2012]. The latter study computed a 7.0 cm global root-mean-square M_2 sea surface elevation error in the deep ocean with respect to the TPXO8-atlas [*Egbert et al.*, 1994]. This error is comparable to errors in other forward tide models employing a parameterized topographic internal wave drag. The frequency spectra of kinetic energy $E(\omega)$ from the model are compared to frequency spectra from historical velocity observations at seven moorings within our North Pacific domain along 175°W and 152°W. The moorings were deployed as part of the Pacific Zonal Exploration Array [*Schmitz*, 1988]. The instruments are located in the upper ocean between 143 and 168 m with record lengths varying between 348 and 705 days and sampling periods ranging from 15 min to 1 h.
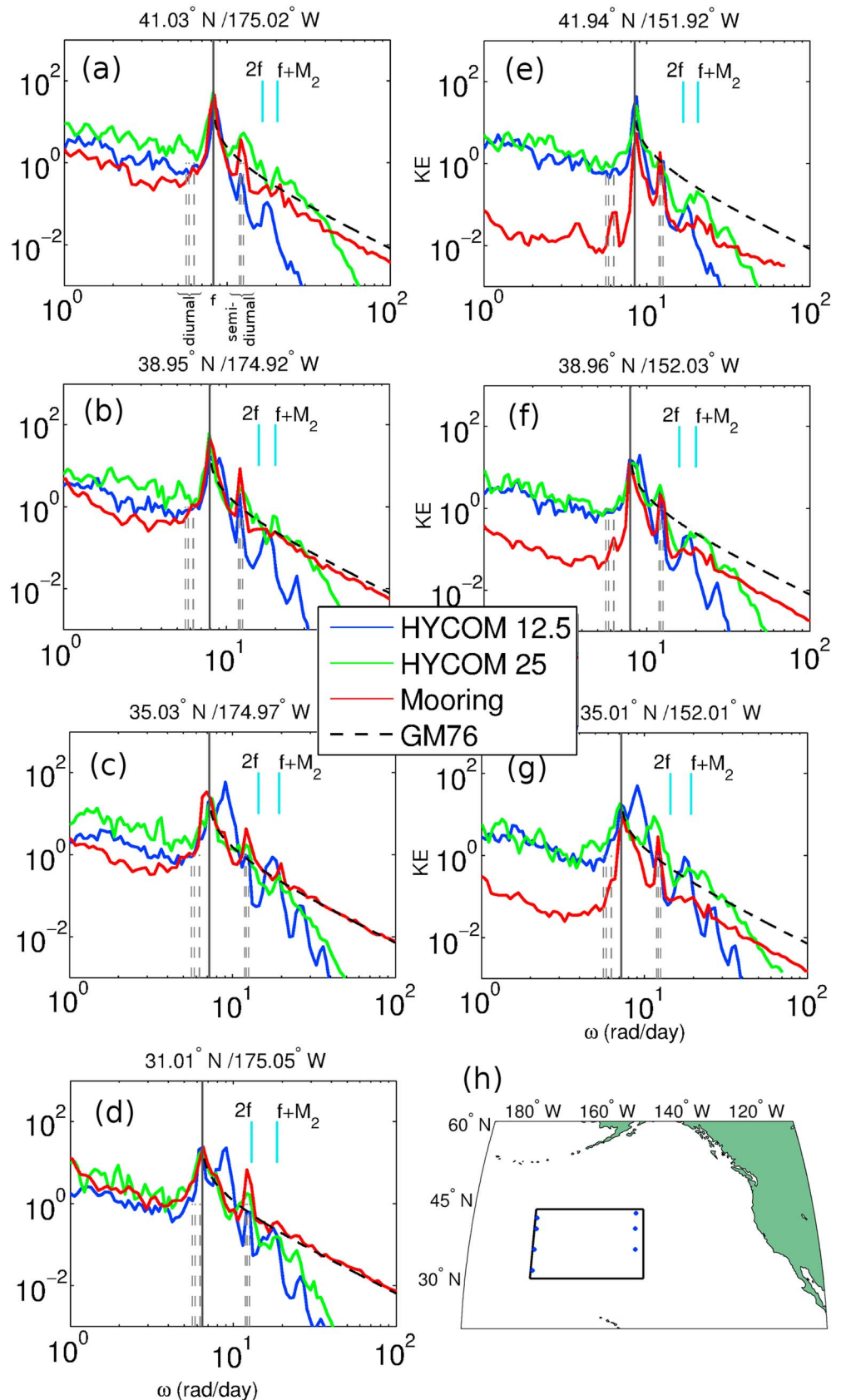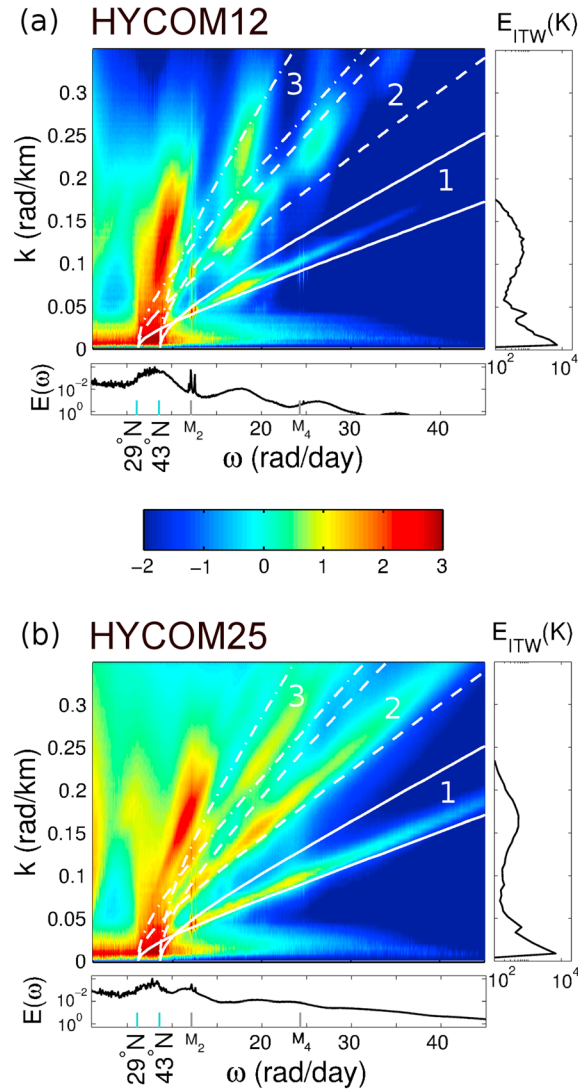
Figure 1

Figure 2. The K-ω spectra of kinetic energy $E(K, \omega)$ {(m/s)^2 [(d)(km)]} on a log$_{10}$ scale for (a) HYCOM12 and (b) HYCOM25. The white curves represent bounding linear dispersion relations of the first three internal wave vertical modes (solid = mode 1; dashed = mode 2; and dash dotted = mode 3). The mode bands are labeled inside the panel with white lettering. Below and to the right of the color-contoured $E(K, \omega)$, the spectra $E(\omega)$ integrated over all horizontal wave numbers K, and $E_{ITW}(K)$ integrated over frequencies larger than the inertial frequency ($\omega \geq f_{29N}$), are shown, respectively. In the $E(\omega)$ spectra, cyan lines indicate the inertial frequencies at the bounding latitudes 29°N and 43°N, while M_2 and M_4 frequencies are also indicated.

3. Derivation of Kinetic Energy Spectra and Nonlinear Spectral Transfers

We compute E and T directly from the surface velocity without employing the QG assumption used in *Scott and Wang* [2005] and *Arbic et al.* [2012b, 2014]. We begin with the momentum equation

$$\frac{\partial \mathbf{u}}{\partial t} + [(\boldsymbol{u} \cdot \nabla)\mathbf{u}] = \text{OT}, \qquad (1)$$

where OT refers to other terms, not considered in the present analysis, and $\boldsymbol{u} = (u, v)$ is the horizontal velocity vector with zonal and meridional components u and v, respectively. Note that in equation (1), we exclude nonlinear terms of the form $w\partial\mathbf{u}/\partial z$, where w is the vertical velocity. Taking the Fourier transform of equation (1), and multiplying by the complex conjugate of the Fourier transform of the horizontal velocity vector, yields a spectral energy equation

$$\frac{\partial}{\partial t}E(K, \omega) = T(K, \omega) + \text{OT}. \qquad (2)$$

Thus, E and T are defined by

$$E(K, \omega) = \frac{1}{2}\hat{\boldsymbol{u}}^* \cdot \hat{\boldsymbol{u}}, \qquad (3)$$

$$T(K, \omega) = Re\left\{-\hat{\boldsymbol{u}}^* \cdot \left[\boldsymbol{u} \cdot \hat{\nabla}\boldsymbol{u}\right]\right\}, \qquad (4)$$

where * denotes complex conjugate, ˆ refers to the Fourier transform, and Re refers to the real part of a complex number. From equation (2), negative (positive) values of $T(K, \omega)$ imply that nonlinear interactions represent a sink (source) of kinetic energy for the given (K, ω). Before the spectral analysis is performed, the time series are detrended and windowed in space and time, following standard procedures of time series analysis.

4. Comparison With Observations

Near-inertial peaks in the $E(\omega)$ kinetic energy spectra at the seven mooring locations are reasonably consistent between the models

Figure 1. (a–g) Frequency spectra $E(\omega)$ of surface kinetic energy {(m/s)^2 (d)} from moored current meter observations (red), HYCOM12 (blue), and HYCOM25 (green) and the GM76 [*Cairns and Williams*, 1976] model spectrum (dashed black). The spectra are logarithmically smoothed for display purposes. GM76 spectra are computed with reference values of total energy of the internal wavefield and stratification set to $E_0 = 6.3e^{-5}$ m^2 s^{-2} and $N_0 = 5.2e^{-3}$ s^{-1}, respectively. Vertical lines are drawn at f, $2f$, and $f + M_2$, while dashed vertical lines are drawn at the four semidiurnal (M_2, S_2, N_2, and K_2) and four diurnal (K_1, O_1, P_1, and Q_1) tidal frequencies forced in the model. (h) The analysis region in the northeast Pacific. The blue stars denote the locations of moored observations used in Figures 1a–1g.
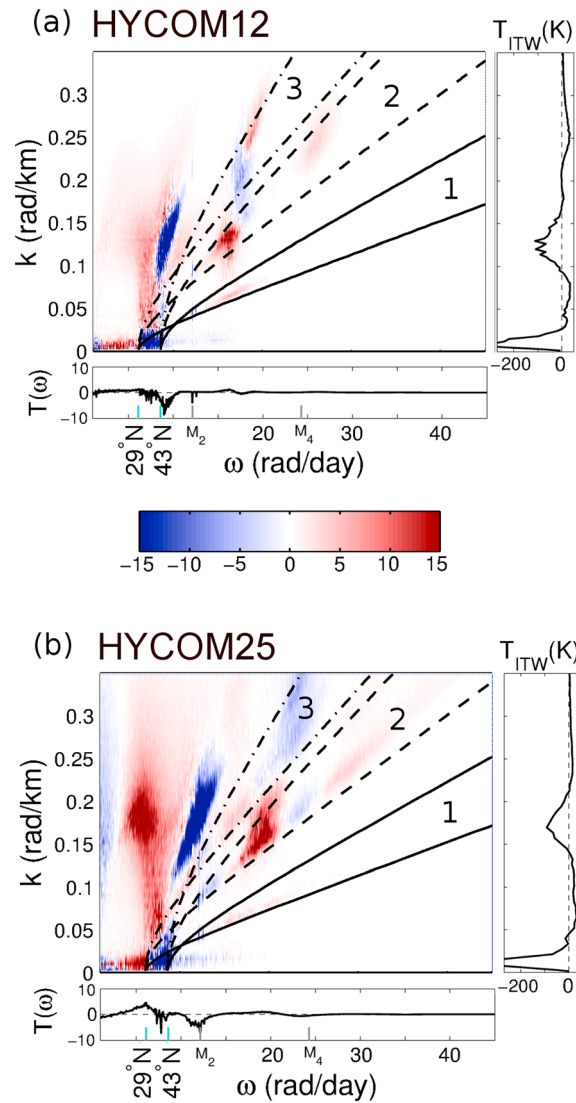
Figure 3. As in Figure 2 but for nonlinear spectral kinetic energy transfer $T(K, \omega)$ {(10^{-9} W/kg) [(d) (km)]}, with linear colorbar and dispersion curves and mode band numbers shown in black. Energy is taken out of the blue regions (low-mode near-inertial and semidiurnal internal waves) and added to the red regions (higher-frequency and higher-wave number internal waves).

and observations (Figures 1a–1g) except for the observation at 41.94°N, 151.92°W, where the HYCOM25 and HYCOM12 peaks are 3 and 9 times larger, respectively, than the observed peak (Figure 1e). This is likely because of different winter storm forcing during the year of the current meter measurements than in the model [*D'Asaro*, 1985]. In the other locations, the near-inertial peaks differ by factors ranging between 0.3 and 2.5 and thus are within an order of magnitude of each other. Diurnal peaks are visible in the observations at the eastern but not western location and not in the models at any location. Semidiurnal tidal peaks are visible in all observational and model spectra shown in Figure 1. Above the semidiurnal tidal frequency, the energy in the observations decreases approximately as ω^{-2}, consistent with the GM76 [*Cairns and Williams*, 1976] spectra. The models, especially HYCOM12, have a steeper roll-off at high frequencies. At super-tidal frequencies, HYCOM25 rolls off less steeply, and thus lies closer to the observations than HYCOM12. We speculate that this is due to better resolution of higher vertical modes, which are required to fill out the internal wave spectrum [*Garrett and Munk*, 1975]. At some locations, HYCOM25 displays peaks at frequencies of $2f$ and $f + \omega_{M2}$ (f refers to the Coriolis frequency and ω_{M2} refers to the M_2 tidal frequency) that are also visible in the observations.

5. Horizontal Wave Number-Frequency Spectra and Spectral Transfers

The spectrum $E(K, \omega)$, along with the dispersion curves of internal waves, are shown in Figure 2. To compute the dispersion curves, we solve for the eigenspeed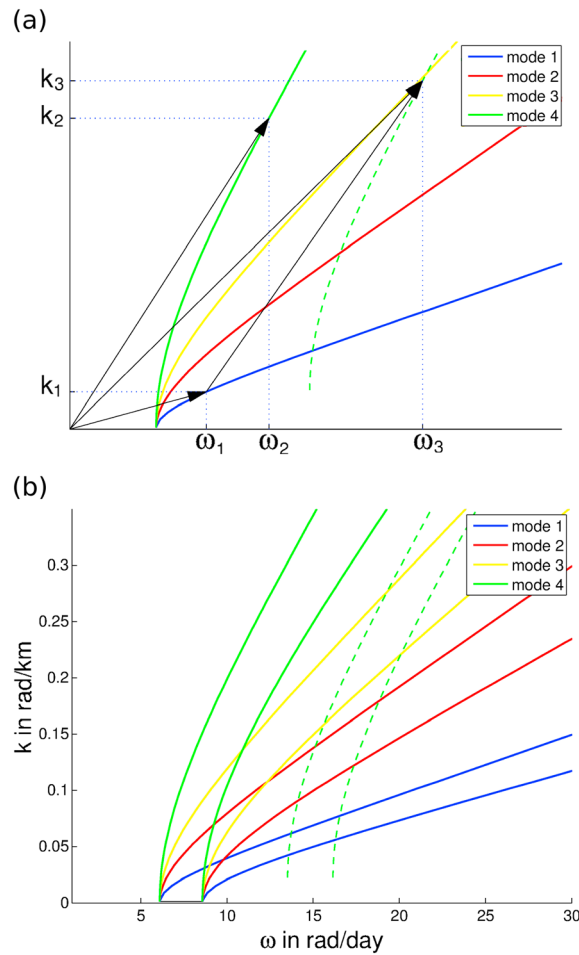s c_n of the nth vertical mode [*Munk*, 1981] using a shooting method code (Glenn Flierl, personal communication, 1995) applied to the internal wave Sturm-Liouville problem. Stratification profiles $N^2(z)$, computed from time-averaged temperatures and salinities at individual grid points from the HYCOM25 output, are taken as inputs to the Sturm-Liouville problem. The dispersion relation for a particular vertical mode is given by

$$\omega^2 = f^2 + c_n^2 K^2. \tag{5}$$

For the analysis region, f varies with latitude and $N^2(z)$ varies from one model grid point to the next. We computed eigenspeeds c_n for each of the first three vertical modes at all model grid points along the 29°N and 43°N bounding latitudes. The bounding dispersion curves for each mode are computed using the minimum c_n value along the northern latitude and the maximum c_n value along the southern latitude. Because all computations made from these high-resolution models are time consuming, we did not separately compute the dispersion curves for the HYCOM12 stratification but use those from HYCOM25.

(a)

(b)

Figure 4. Sketch of internal wave-wave triad interactions in K-ω space. (a) The dispersion relations of four internal wave vertical modes. The cross section of the green dashed and yellow lines illustrates the triad interaction, where mode 1 and mode 4 internal waves form a mode 3 internal wave with the frequency ω_3 and wave number k_3. (b) Equivalent approach as in Figure 4a but applied to a band of internal wave dispersion relations given by a range of geographical latitudes and vertical stratification profiles.

The models' K-ω spectra (Figure 2) display lobes between the bounding dispersion curves. Because of the higher resolution of HYCOM25, its kinetic energy spectrum $E(K, \omega)$ has higher energy levels extending to smaller spatial and temporal scales than HYCOM12. Both models exhibit the largest spectral kinetic energy in the inertial frequency range, defined by the 29°N–43°N bounding latitudes of the analysis region. Further, energy accumulation is found along the dispersion relations for higher vertical modes. The peaks for high vertical modes are centered at horizontal wavelengths of about 50 km (0.125 rad/km) and 37 km (0.170 rad/km) for HYCOM12 and HYCOM25, respectively. In the $E(K, \omega)$ spectra, the semidiurnal tidal lines are visible at around 12 rad/d and peak within the bounding dispersion relations for modes 1, 2, and 3 with approximate wavelengths of 144, 72, and 50 km, respectively. However, substantial energy is found between those peaks, not covered by the range of modal dispersion relations. The spectra $E(\omega)$ integrated over all wavelengths also display semidiurnal peaks. Tidal harmonics, such as M_4, are seen in the HYCOM12 spectrum. Diurnal tides are not readily apparent in the frequency spectra $E(\omega)$. In addition, we present kinetic energy spectra $E_{ITW}(K)$ integrated over all frequencies higher than the inertial frequency at the lower boundary of the region. Thus, $E_{ITW}(K)$ represents the horizontal wave number spectra for internal wave horizontal kinetic energy. In $E_{ITW}(K)$, a peak is visible at the 0.044 rad/km wave number corresponding to the mode 1 internal tide.

The nonlinear spectral kinetic energy transfer $T(K, \omega)$ is displayed in Figure 3. The largest negative (sink) values of the nonlinear spectral kinetic energy transfer $T(K, \omega)$ show energy being transferred out of the low-wave number near-inertial and supermode 3 semidiurnal bands in HYCOM25 (Figure 3b), the latter coinciding with the large high-mode $E(K, \omega)$ values discussed earlier. The negative $T(K, \omega)$ values imply that nonlinearities extract energy from these regions of the K-ω spectrum to feed other spectral regions. The largest positive (source) $T(K, \omega)$ shows energy being transferred into the supermode 3 near-inertial and mode 2 $2f$ bands in HYCOM25. As with the spectra $E(K, \omega)$, large $T(K, \omega)$ extends to higher wave numbers and frequencies in HYCOM25 than HYCOM12, demonstrating that nonlinear interactions are more active in HYCOM25. Also as in $E(K, \omega)$, the semidiurnal internal tides are visible as lines in $T(K, \omega)$ and $T(\omega)$, with segments of increased energy transfer coinciding with the ranges given by the respective dispersion relations.

Along the 29°N southern boundary of the domain, the internal wave transfer rates $T_{ITW}(K)$ has a large negative (sink) peak at wavelengths larger than approximately 300 km. The dominant motions contributing to this sink are near inertial. For wavelengths less than 300 km, $T_{ITW}(K)$ is characterized by a small positive (source) peak followed by a larger negative (sink) peak at still higher wave numbers. While the peak at wavelengths larger than 300 km is consistent between HYCOM12 and HYCOM25, the

structure at higher wave numbers differs between the two simulations with the peak shifting from approximately 50 km in HYCOM12 to 35 km in HYCOM25.

6. Triad Interaction in Wave Number-Frequency Space

An interpretation for the structures seen in $E(K, \omega)$ (Figure 2) and $T(K, \omega)$ (Figure 3) is obtained by considering wave triad interactions [*McComas and Bretherton*, 1977], where we assume that a mode 1 internal wave with frequency ω_1 and wave number k_1 interacts with a mode 4 wave (Figure 4a). To visualize possible triad interactions, the mode 4 dispersion relation is translated in K-ω space by (k_1, ω_1) as denoted by the green dashed line. Permitted interactions are given by intersections of the translated dispersion relation with the dispersion relation of internal waves. As an example, we choose the intersection with the mode 3 dispersion relation, from which (k_2, ω_2) and (k_3, ω_3), the frequencies and wave numbers of the interacting and resulting internal waves, respectively, are then specified. By definition, the resulting wave fulfills $k_3 = k_1 \pm k_2$ and $\omega_3 = \omega_1 \pm \omega_2$. Note that Figure 4a is schematic in nature—for simplicity, we have not accounted for all low-mode interactions nor the additional complication that horizontal wave number is a vector and not a scalar quantity.

Interpretation of triad interactions in K-ω space can be extended to dispersion relation bands instead of lines (Figure 4b). The bands appear because of the range of f and N in the considered region as described in the previous section. The intersections consist of regions which appear through overlapping of the translated dispersion relation. The intersecting regions appear as the patchy structures in plots of $E(K, \omega)$ (Figure 2) and $T(K, \omega)$ (Figure 3). Integration over these fields yields a wavey rather than a monotonically decreasing $E(\omega)$ spectrum (Figure 2) especially apparent in HYCOM12. This can be interpreted as the results of triad interactions of a limited number of low-mode internal waves. Since our models differ in horizontal resolution, patches in the HYCOM12 and HYCOM25 plots differ in detail but arise from the same physical mechanism. We expect that the strength and number of triad interactions will increase with finer model resolution.

7. Summary and Conclusion

In this paper, we spectrally analyzed the surface horizontal velocities of two HYCOM simulations with 0.08° and 0.04° horizontal resolution, respectively, that are forced simultaneously by atmospheric fields and astronomical tides. We analyzed a two-dimensional region in the northeast Pacific north of the Hawai'ian Islands, and horizontal wave number-frequency K-ω spectra of horizontal kinetic energy and nonlinear energy transfers are computed and interpreted. The K-ω spectra of E and T show clear signatures along the dispersion relations of the low-vertical-mode internal waves. The internal tides are visible as stripes in the K-ω spectra and peak at the wavelengths consistent with estimates from linear internal wave theory. HYCOM25 has larger values of E and T at smaller spatial and temporal scales than does HYCOM12. Comparisons of model frequency spectra with seven moored current meter observations suggest that the finer-resolution HYCOM25 simulation is more realistic than HYCOM12.

We conclude from this study that calculating the spectral nonlinear kinetic energy transfer in K-ω space is a useful technique to analyze and interpret simulated internal wave dynamics. The models reproduce low-vertical-mode internal wave triad interactions. The spectral transfers demonstrate that energy is extracted from low-wave number near-inertial and supermode 3 tidal motions in order to feed a supermode 3 near-inertial continuum and mode 2 $2f$ peak in the internal wave spectrum. The patchy structure of the spectra can be interpreted as triad interactions of a limited number of low-mode internal waves. It will be interesting to follow up this study with analyses of three-dimensional model fields and of higher-resolution simulations, which are likely to further expand the realism of the internal wave spectrum in global ocean models.

References

Arbic, B. K., A. J. Wallcraft, and E. J. Metzger (2010), Concurrent simulation of the eddying general circulation and tides in a global ocean model, *Ocean Model.*, *32*, 175–187.

Arbic, B. K., J. G. Richman, J. F. Shriver, P. G. Timko, E. J. Metzge, and A. J. Wallcraft (2012a), Global modeling of internal tides within an eddying ocean general circulation model, *Oceanography*, *25*, 20–29.

Arbic, B. K., R. B. Scott, G. R. Flierl, A. J. Morten, J. G. Richman, and J. Shriver (2012b), Nonlinear cascades of surface oceanic geostrophic kinetic energy in the frequency domain, *J. Phys. Oceanogr.*, *42*, 1577–1600.

Arbic, B. K., M. Müller, J. G. Richman, J. F. Shriver, A. J. Morten, R. B. Scott, G. Sérazin, and T. Penduff (2014), Geostrophic turbulence in the frequency-wave number domain: Eddy-driven low-frequency variability, *J. Phys. Oceanogr.*, *44*, 2050–2069.

Cairns, J. L., and G. O. Williams (1976), Internal wave observations from a midwater float, 2, *J. Geophys. Res.*, *81*(12), 1943–1950, doi:10.1029/JC081i012p01943.

Chassignet, E. P., et al. (2009), US GODAE: Global ocean prediction with the HYbrid Coordinate Ocean Model (HYCOM), *Oceanography*, *22*, 64–75.

D'Asaro, E. A. (1984), Wind forced internal waves in the North Pacific and Sargasso Sea, *J. Phys. Oceanogr.*, *14*, 781–794.

D'Asaro, E. A. (1985), The energy flux from the wind to near-inertial motions in the surface mixed layer, *J. Phys. Oceanogr.*, *15*, 1043–1059.

Egbert, G. D., A. F. Bennett, and M. G. G. Foreman (1994), TOPEX/POSEIDON tides estimated using a global inverse model, *J. Geophys. Res.*, *99*(C12), 24,821–24,852, doi:10.1029/94JC01894.

Garrett, C., and E. Kunze (2007), Internal tide generation in the deep ocean, *Annu. Rev. Fluid Mech.*, *39*, 57–87.

Garrett, C. J. R., and W. H. Munk (1975), Space-time scales of internal waves. A progress report, *J. Geophys. Res.*, *80*, 291–297, doi:10.1029/JC080i003p00291.

MacKinnon, J. A., M. H. Alford, O. Sun, R. Pinkel, Z. Zhao, and J. Klymak (2013), Parametric subharmonic instability of the internal tide at 29°N, *J. Phys. Oceanogr.*, *43*, 17–28.

McClean, J. L., A. J. Semtner, and V. Zlotnicki (1997), Comparisons of mesoscale variability in the Semtner-Chervin 1/4° model, the Los Alamos Parallel Ocean Program 1/6° model, and TOPEX/POSEIDON data, *J. Geophys. Res.*, *102*(C11), 25,203–25,226, doi:10.1029/97JC01222.

McComas, C. H., and F. P. Bretherton (1977), Resonant interaction of oceanic internal waves, *J. Geophys. Res.*, *82*(9), 1397–1412, doi:10.1029/JC082i009p01397.

Müller, M., J. Y. Cherniawsky, M. G. G. Foreman, and J.-S. von Storch (2012), Global M2 internal tide and its seasonal variability from high resolution ocean circulation and tide modeling, *Geophys. Res. Lett.*, *39*, L19607, doi:10.1029/2012GL053320.

Müller, P., G. Holloway, F. Henyey, and N. Pomphrey (1986), Nonlinear interactions among internal gravity waves, *Rev. Geophys*, *24*(3), 493–536, doi:10.1029/RG024i003p00493.

Munk, W. (1981), Internal waves and small-scale processes, in *Evolution of Physical Oceanography: Scientific Surveys in Honor of Henry Stommel*, edited by B. A. Warren and C. Wunsch, pp. 264–291, The MIT Press, Cambridge and London.

Munk, W., and C. Wunsch (1998), Abyssal recipes II: Energetics of tidal and wind mixing, *Deep Sea Res., Part I*, *45*, 1977–2010.

Polzin, K. (2004), Heuristic description of internal wave dynamics, *J. Phys. Oceanogr.*, *34*, 214–230.

Polzin, K. L., A. C. Naveira Garabato, T. N. Huussen, B. M. Sloyan, and S. Waterman (2014), Fine-scale parameterizations of turbulent dissipation, *J. Geophys. Res. Oceans*, *119*, 2169–9291, doi:10.1002/2013JC008979.

Schmitz, W. J., Jr. (1988), Exploration of the eddy field in the midlatitude North Pacific, *J. Phys. Oceanogr.*, *18*, 459–468.

Scott, R. B., and F. Wang (2005), Direct evidence of an inverse kinetic energy cascade from satellite altimetry, *J. Phys. Oceanogr.*, *35*, 1650–1666.

Shriver, J. F., B. K. Arbic, J. G. Richman, R. D. Ray, E. J. Metzger, A. J. Wallcraft, and P. G. Timko (2012), An evaluation of the barotropic and internal tides in a high-resolution global ocean circulation model, *J. Geophys. Res.*, *117*, C10024, doi:10.1029/2012JC008170.

Silverthorne, K. E., and J. M. Toole (2009), Seasonal kinetic energy variability of near-inertial motions, *J. Phys. Oceanogr.*, *39*, 1035–1049.

Simmons, H. L., and M. H. Alford (2012), Simulating the long-range swell of internal waves generated by ocean storms, *Oceanography*, *25*, 30–41.

Sugiyama, Y., Y. Niwa, and T. Hibiya (2009), Numerically reproduced internal wave spectra in the deep ocean, *J. Geophys. Res.*, *36*, L07601, doi:10.1029/2008GL036825.

Sun, O. M., and R. Pinkel (2013), Subharmonic energy transfer from the semidiurnal internal tide to near-diurnal motions over Kaena Ridge, Hawaii, *J. Phys. Oceanogr.*, *43*, 766–789.

Timko, P. G., B. K. Arbic, J. G. Richman, R. B. Scott, E. J. Metzger, and A. J. Wallcraft (2013), Skill testing a three-dimensional global tide model to historical current meter records, *J. Geophys. Res. Oceans*, *118*, 6914–6933, doi:10.1002/2013JC009071.